HYDROLOGICAL PROCESSES
Hydrol. Process. (2010)
Published online in Wiley Online Library
(wileyonlinelibrary.com) DOI: 10.1002/hyp.7882

A numerical study of the rainstorm characteristics of the June 2005 flash flood with WRF/GSI data assimilation system over south-east China

Qilin Wan[1] and Jianjun Xu[2]*

[1] *Institute of Tropical and Marine Meteorology, CMA, Guangzhou 510080, China*
[2] *IMSG at NOAA/NESDIS/STAR, WWB, Room 602, 5200 Auth road, Camp Springs, MD 20764, USA*

Abstract:

The evolution and structure of rainstorms associated with a flash-flood event are simulated by the Advanced Weather Research and Forecasting (WRF-ARW) model of the National Center for Atmospheric Research and the Gridpoint Statistical Interpolation (GSI) data assimilation (DA) system of the National Oceanic and Atmospheric Administration (NOAA) of the United States. The event is based on a flash flood that occurred in the central Guangdong Province of south-east China during 20–21 June 2005. Compared to an hourly mixed rain-gauge and satellite-retrieved precipitation data, the model shows the capability to reproduce the intensity and location of rainfall; however, the simulation depends on three conditions to a large extent: model resolution, physical processes schemes and initial condition. In this case, the Eta Ferrier microphysics scheme and the initialization with satellite radiance DA with a fine 4-km grid spacing nested grid and coarse 12-km grid spacing outer grid are the best options. The model-predicted rain rates, however, are slightly overestimated, and the activities of the storms do not precisely correspond with those observed, although peak values are obtained. Abundant moisture brought by the south-westerly winds with a mesoscale low-level jet from the South China Sea or Bay of Bengal and trapped within the XingfengJiang region encompassed by northern Jiulian, southern Lianhua and eastern small mountains are apparently the primary elements responsible for the flood event. All simulated rainstorms were initiated over the southern slopes of the Jiulian Mountain and moved south or north-eastward within the Xingfengjiang region. Meanwhile, the Skew-T/Log-P diagrams show that there is a fairly high convective available potential energy (CAPE) over the active areas of the rainstorms. The higher CAPE provides a beneficial thermodynamic condition for the development of rainstorms, but the higher convective inhibition near the northern, eastern and southern mountains prohibits the storms from moving out of the region and causes heavy rainfall that is trapped within the area. Copyright © 2010 John Wiley & Sons, Ltd.

KEY WORDS rainstorm; flash flood; numerical study

Received 28 January 2010; Accepted 19 August 2010

INTRODUCTION

Summertime strong convective storms over south-east China are frequently associated with the presence of tropical air that arrives as part of the East Asian summer monsoon (EAM, Zhu *et al*., 1981). The subtropical regions of south-east China encompass complex topography (Figure 1), including ocean, mountain ranges and diverse land-surface characteristics. With the arrival of the EAM, severe storms can occur and can result in hydrological disasters such as flash flooding. In this season, a quasi-stationary front, the Mei-Yu front, is formed and it extends from eastern China to southern Japan. The Mei-Yu front is one of the most significant circulation systems for the hydrological cycle in the East Asia monsoon region. Many previous studies (Mcanelly and Cotton, 1986; Zhang *et al*., 1986; Ding, 1992, Chen *et al*., 1998; Zhang *et al*., 2003, Li *et al*., 2003) have indicated the heavy precipitation events, which were primarily associated with mesoscale convective systems (MCSs), organized on the meso-α scale (200–2000 km, >6 h) (Maddox, 1980). Very intense and concentrated rainfall events are often associated with organized mesoscale disturbances embedded within and propagating along the Mei-Yu front (Fang, 1985).

The MCS with meso-α scale consists of a few meso-β storms with a scale of 20–200 km. The structure and evolution of the rainstorms with meso-β scales are not clearly known because the routine radiosonde data do not have sufficient spatial and temporal resolution to resolve these small-scale systems. The high-resolution satellite-retrieved rainfall data combined with rain-gauge data (Liang and Xie, 2006, personal communication) during the period of a heavy rainfall event occurring in south-east China in June 2005, together with the capability of an advanced mesoscale model, allow the possibility of studying this kind of MCS. The evolution, structure and dynamic and thermodynamic conditions associated with the heavy rainstorm are discussed in this study.

The data used in this study are given in the Section 'Precipitation Dataset'. The Section 'Synoptic Situation of the Event' presents a brief overview of the synoptic situation related to the event. The Advanced Weather

* Correspondence to: Jianjun Xu, IMSG at NOAA/NESDIS/STAR, WWB, room 602, 5200 auth road, Camp Springs, MD 20764, USA. E-mail: Jianjun.xu@noaa.gov

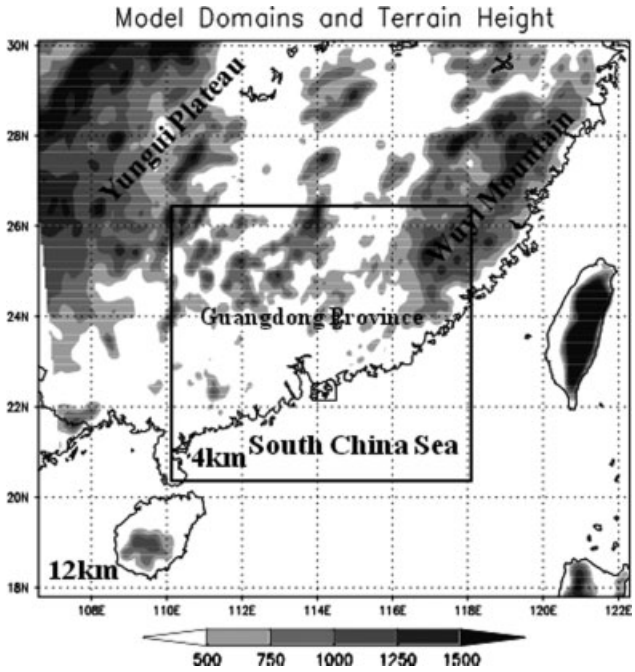

Figure 1. Domains for the ARW-WRF forecasts. The outer box is the coarse grid (domain 1) with a resolution of 12 km; the inner box is the nested grid (domain 2) with a resolution of 4 km. The shading shows the terrain elevation (m)

Research and Forecasting (WRF-ARW) model (Skamarock *et al*., 2005) and its option of model resolution, physical scheme and initialization are described in Section 'The Mesoscale Model'. Section 'Observation of the Rainstorms and Precipitation' presents the observations of the meso-β scale convective system. The evolution and structure of the convective system are analysed in Section 'The Model Simulation' and the possible causes of the flash-flood event are discussed in Section 'The Relationship between Rainstorm and Mesoscale Low-Level Jet'. Finally, the summary and discussion are given in 'Summary' Section.

PRECIPITATION DATASET

An hourly precipitation data with $0{\cdot}125^\circ \times 0{\cdot}125^\circ$ grid spacing was employed in this study, which was created by the Climate Prediction Center (CPC) morphing method (CMORPH) (Joyce *et al*., 2004) with an hourly precipitation data derived from satellite observation and hourly rain-gauge dataset. The rain-gauge stations are shown in Figure 2a, which includes 394 stations over the Guangdong Province in south-east China.

The 24-h accumulated precipitation over the central Guangdong Province from 06Z20 to 06Z21 June 2005 is depicted in Figure 2b. The evidence shows that the 24-h accumulated rainfall exceeding 100 mm appeared over the central Guangdong Province (e.g. XingfengJiang region, which is surrounded by northern Jiulian, southern Lianhua and eastern small mountains). The maximum (up to 350 mm) rainfall appeared near a reservoir in the Xingfengjiang region (Figure 2b). The rain band displays the direction from south-west to north-east. According to the historic record reported by the Guangdong Province observational center, this heavy precipitation episode was the third most severe flood event in this area since 1950, which resulted in 65 deaths and $400 million in property damage.

SYNOPTIC SITUATION OF THE EVENT

Before the flood broke out, there was a ridge of high pressure at 00Z20 June 2005 of 500 hPa (Figure 3a) starting from the western Pacific subtropical areas, moving along the south-west border of the Chinese mainland and ending in northern Bangladesh. The high-pressure system is often called *Western Pacific Subtropical Highs (WPSHs)*. Under the control of the WPSH system, a strong south-westerly flow appeared towards the northern or north-western sides of the high-pressure ridge. At mid-latitude, a major trough was located over north-eastern China. There was another short-wave trough towards the south-west, located along 110 °E, with weak cold dry air merging into the flow above the sub-tropical south-westerly. Consequently, the relatively cold dry air took over the central Guangdong Province areas, where a flood event was about to occur. Consistent with the middle–upper atmosphere situation, the synoptic diagram at the lower level 850 hPa (Figure 3b) shows that a ridge of high pressure was also present over the western Pacific subtropical areas, but it stopped by the western bank of the South China Sea and its position was located towards the south of the ridge aloft. Meanwhile, a wind shear line emerged over southern China extending from 100 °E to the western Pacific off the south coast of Japan. Between the ridge line and the wind shear line, there was a south-westerly synoptic-scale low-level jet (LLJ) with wind speeds of over 12 m s^{-1} from the South China Sea to the Bay of Bengal. The northern edge of the synoptic LLJ is located over the axis of the rain band (Figure 2b). Apparently, the lower level of the flooding area was dominated by relatively warm moist air.

This vertical synoptic structure with the lower warm wet flow and the middle upper cold dry air provided a beneficial unstable condition for a convective system, with an inverted trough moving eastwards across these areas. The sounding diagram (Figure 4) at 06Z20 June located near the reservoir in the Xingfengjiang region indicates (Figure 4) that precipitable water in the area exceeded 58 mm, the convective available potential energy (CAPE) exceeded 1000 J kg^{-1} and the convective inhibition (CIN) was almost zero; this furthermore reflects the existence of a conditional unstable situation.

THE MESOSCALE MODEL

WRF-ARW model and model resolution

The numerical model used in this study is the WRF-ARW, which is a non-hydrostatic, fully compressible, primitive equation model. Lead institutions involved

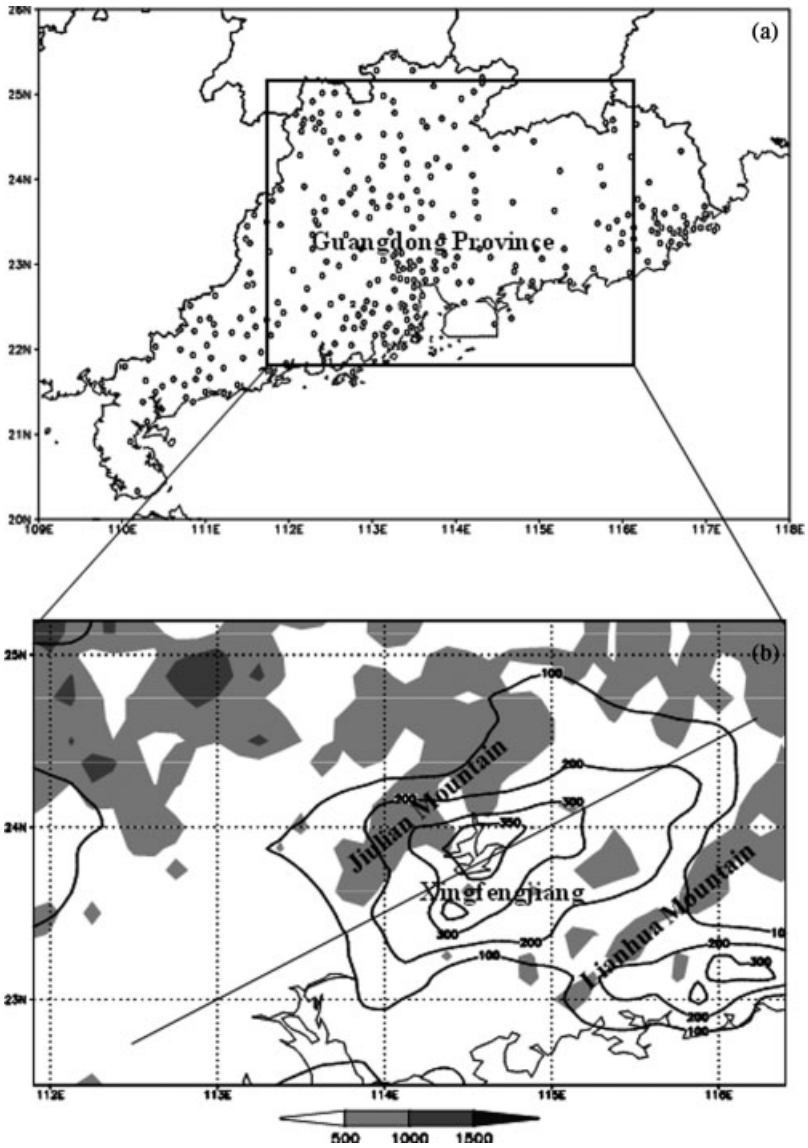

Figure 2. (a) The distribution of rain-gauge stations over Guangdong Province in south-east China. (b) Observed 24-h accumulated precipitation from 06Z20 to 06Z21 June 2005 based on mixed rain-gauge and satellite-retrieved precipitation data (mm). Shading indicates the terrain elevation (m). The central bird-like contour is a reservoir within the Xingfengjiang region surrounded by northern Jiulian, southern Lianghua and eastern small mountains. The slope line indicates the axis of the rain band

in the effort include the National Center for Atmospheric Research (NCAR), the Air Force Weather Agency (AFWA), the National Oceanic and Atmospheric Administration (NOAA) and other governmental agencies and universities. WRF is built around a software architectural framework in which different dynamical cores and model physics packages are accessible within the same code. Within the WRF framework, it is possible to mix the dynamical cores with differing physics packages to optimize the performance as each core has strengths and weaknesses in different areas.

In accordance with the multiple options for WRF-ARW model packages, we first choose an appropriate model resolution. During the last two decades, the meteorological community has paid great attention to the effects of the model horizontal resolution on forecast accuracy (Mass *et al*., 2002). For example, Weisman *et al*. (1997), using a non-hydrostatic model to simulate a mid-latitude squall line at horizontal grid spacing ranging from 1 to 12 km, found that the development of the squall line became more realistic as resolution increased, and that the 4-km grid spacing successfully duplicated much of the observed mesoscale structure and evolution. Gallus (1999) examined the variation in the precipitation forecast skill of the Eta model for three heavy summertime precipitation events as the grid spacing was decreased from 79 to 12 km. He found that when convective parameterization schemes were active and produced the bulk of the precipitation, increasing the resolution had little benefit. In order to get a suitable model resolution for the current event, we made a comparison experiment with two pairs of nested domains: one of the nested domains had fine resolution with 4 km and coarse with 12 km (Figure 1) and the other one had 10 km of fine and 30 km of coarse domain (not shown). Figure 5 shows that in the 24 h (from 06Z20 to 06Z21 June, 2005) of

simulated precipitation, the maximum simulated rainfall in the 12- or 30-km model grid spacing (Figure 5b and c) is apparently lower than the observed value. In contrast, the maximum rainfall goes up to 400 mm in the simulation with 4-km grid spacing (Figure 5a), which is the closest to the observed precipitation, although its value is overestimated slightly. A subtle mesoscale characteristic with a scale range from 20 to 200 km is identified significantly. However, it is worth noting that the location of simulated maximum rainfall is about 80 km south-west of the observed. This implies that the 4-km grid spacing is an appropriate option for the current event despite the fact that the option is not perfect, which is discussed in the 'Initialization and Data Assimilation' Section.

Physical processes schemes

Physical processes schemes are another important issue for the WRF-ARW model simulation. Table I describes the options of microphysics, cumulus convection, radiation, land-surface scheme and planetary boundary layer scheme. On the basis of the current event, we concentrate on the microphysics and cumulus schemes in this section. Similar to the other mesoscale model, such as the Pennsylvania State University-National Center for Atmospheric Research (Penn State-NCAR) Mesoscale Model version 5 (MM5), the University of Oklahoma Advance Regional Prediction System (ARPS) and the Colorado State Regional Atmospheric Modeling System (RAMS), there are many options for physical processes schemes in the WRF-ARW model. Some previous studies (Wang and Seaman, 1998; Giorgi and Shields, 1999; Xu and Small, 2002 and many others) have indicated that the option of these schemes has a substantial impact on the simulation. Therefore, we provide the information to support our options. Figure 6 shows the 24-h accumulated precipitation in the simulation of the 4-km model resolution with two options of microphysics schemes: WSM 3-class simple ice scheme (Hong *et al*., 1998) and WSM 6-class graupel scheme (Hong *et al*. 2004). Compared to the simulation in the Eta Ferrier microphysics scheme (Figure 5a) and the observed precipitation (Figure 2b), the simulations in both options totally fail to produce the precipitation distribution of the heavy rainstorm. Similar to the two options mentioned above, all simulations in the other four options, including schemes of Kessler (1969), Lin *et al*. (1983), WSM 5-class scheme (Hong *et al*., 2004) and Thompson *et al*. (2004), do not show the observed precipitation (not shown). The Eta Ferrier microphysics scheme is the best option for the current case study. Figure 7 shows the 24-h accumulated precipitation in the simulation of the 4-km model resolution with two options of cumulus schemes: Grell–Devenyi (2002) ensemble scheme and simplified Arakawa–Schubert scheme (Skamarock *et al*., 2005). Compared to the simulation in the new Kain–Fritsch scheme (Figure 5a), the results indicate that the Grell–Devenyi ensemble scheme completely misses the location of the observed precipitation and the amount of precipitation in the simplified Arakawa–Schubert scheme goes up to 500 mm, which overestimates the observed precipitation substantially. The amount of precipitation in the Betts–Miller–Janjic

Table I. Model options

Physics options	Model set-up
Microphysics	Eta Ferrier microphysics (Ferrier, 1994)
Cumulus	New Kain-Fritsch cumulus scheme (Kain and Fritsch, 1993)
Short-wave radiation	Simple short-wave radiation (Dudhia, 1989)
Long-wave radiation	RRTM long-wave radiation (Mlawer *et al*., 1997)
Planetary boundary layer	Yonsei University (YSU) scheme (Hong *et al*., 1996)
Land-surface model	5-Layer thermal diffusion (Skamarock, 2005)

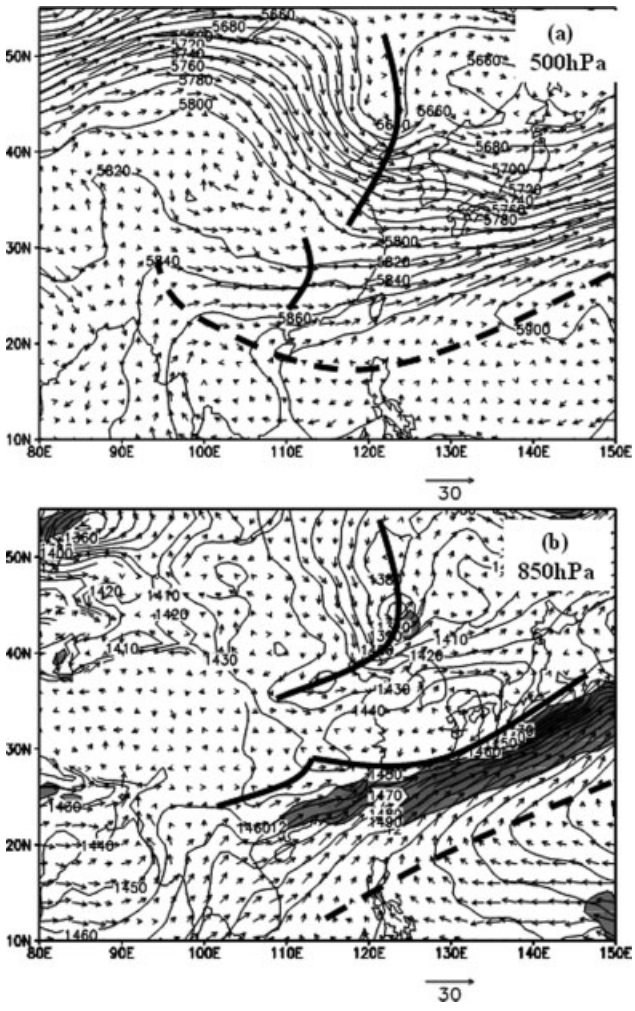

Figure 3. NCEP/NCAR reanalysis for the wind, geopotential height (gpm) fields at 00Z20 June 2005 (a) 500 hPa and (b) 850 hPa. The solid lines depict trough of low pressure. The dashed lines indicate the ridge of high pressure and the shading is the LLJ with wind speed of 12 m s^{-1}

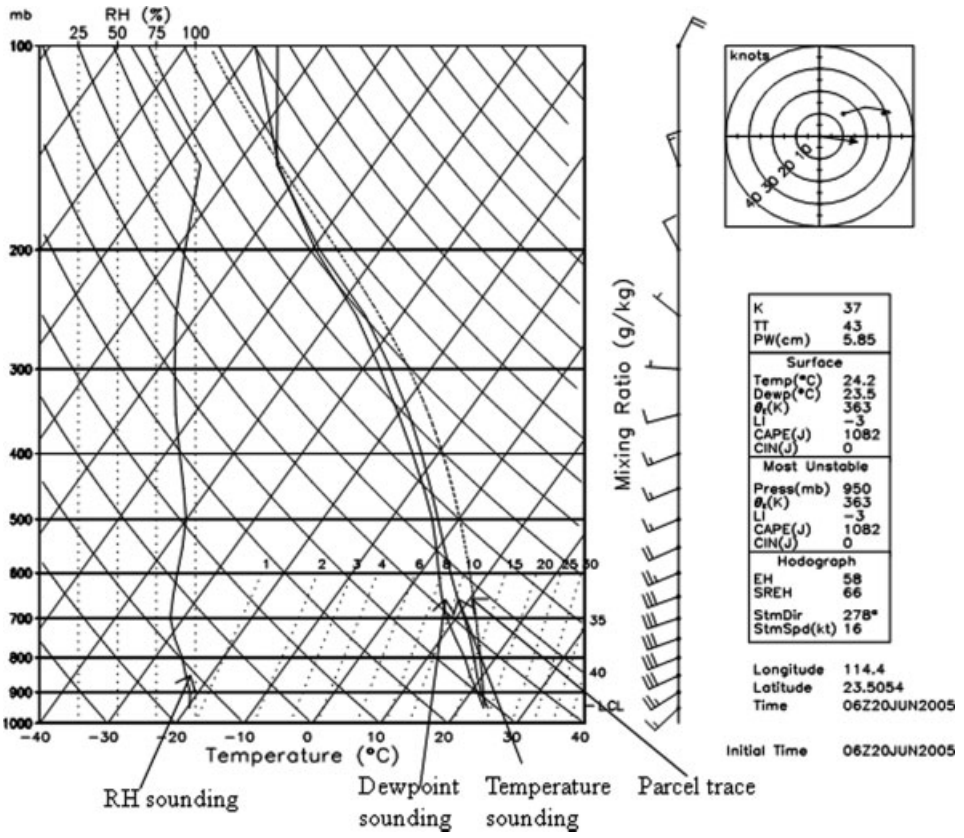

Figure 4. Upper-air sounding near to a station (23·5 °N, 114·4 °E) in Xingfengjiang region at 06Z20 June 2005

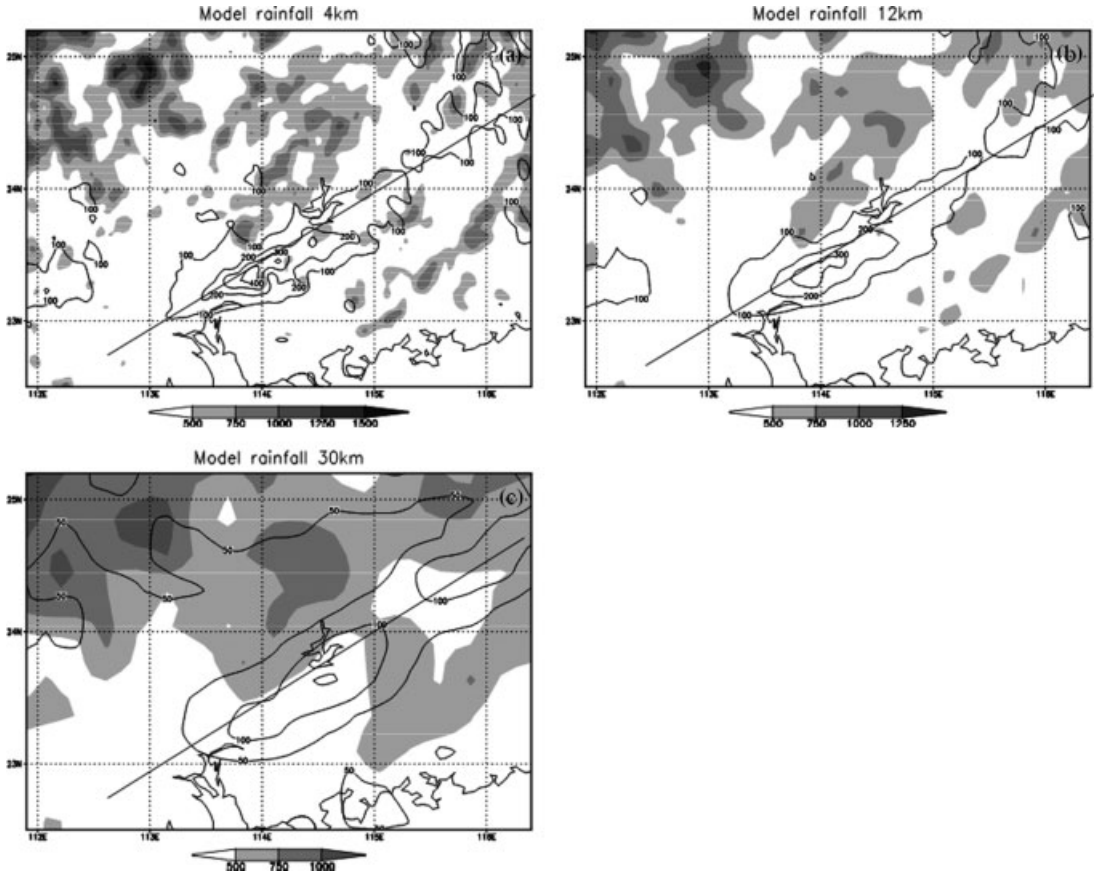

Figure 5. Simulated 24-h accumulated rainfall varying with model resolution from 06Z20 to 06Z21 June 2005. (a) 4 km, (b) 12 km and (c) 30 km. The physical locations are identified by the same tags as those in Figure 2b

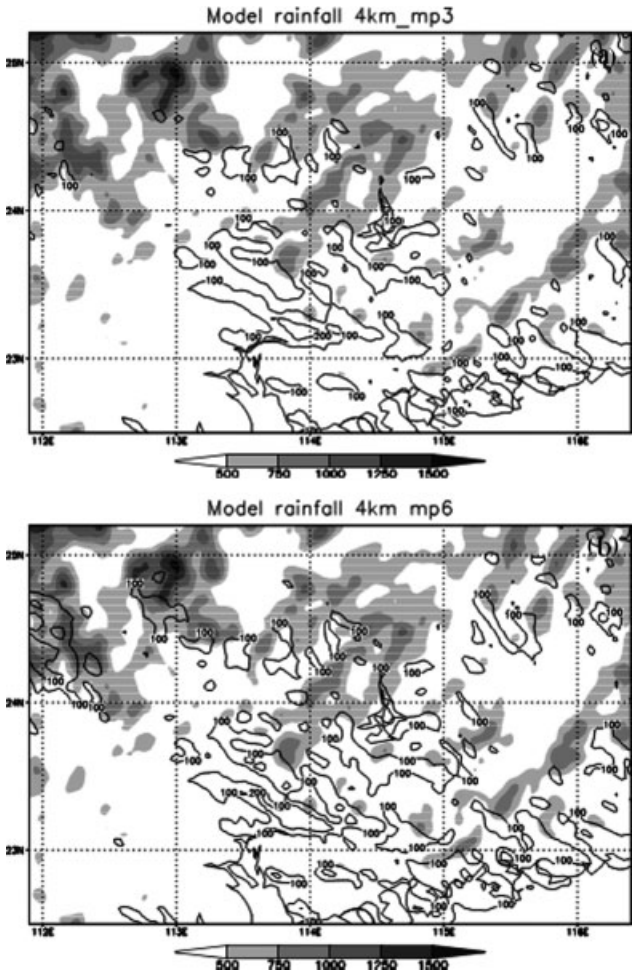

Figure 6. Simulated 24-h accumulated rainfall varying with microphysics schemes from 06Z20 to 06Z21 June 2005. (a) WSM 3-class simple ice scheme and (b) WSM 6-class graupel scheme. The physical locations are identified by the same tags as those in Figure 2b

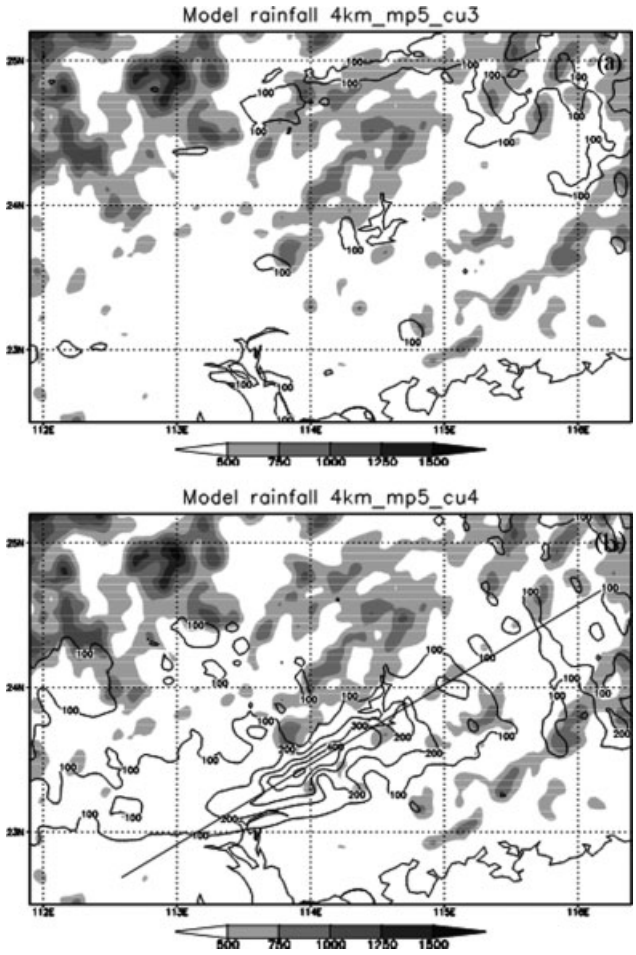

Figure 7. Simulated 24-h accumulated rainfall varying with cumulus schemes from 06Z20 to 06Z21 June 2005. (a) Grell–Devenyi ensemble scheme and (b) simplified Arakawa–Schubert scheme. The physical locations are identified by the same tags as those in Figure 2b

scheme (Betts and Miller, 1986) is much lower than that in the observed scheme (not shown).

Initialization and data assimilation

The initialization is the third issue in this study. The simulation initiates at 06Z20 June 2005 and makes a 24-h run by 06Z21 June. The data for the original initial conditions and time-varying boundary conditions for the coarse domain are taken from the NCEP/NCAR reanalysis data sets with $1^\circ \times 1^\circ$ resolution. Initial conditions include atmospheric and surface fields. According to the above suggestions, the new Kain–Fritsch cumulus scheme and the Eta Ferrier microphysics scheme are good options for the current event; however, the results indicate that the simulation in the above options (Figure 5a) still does not show the right location of rainfall. This clearly reflects that the errors of model simulation are caused by many other reasons besides model resolution and physical schemes. One of the reasons is the initial conditions (Lorenz, 1963; Zhang, 1986; Xu *et al*., 2006; Gallus and Bresch, 2006 and many others). Zhang (1986) noted that, without a proper initial condition, the development of a mesoscale feature within a model could be subject to large errors in timing, location and magnitude. In order to get a better initial condition, the direct radiance assimilation through the gridpoint statistical interpolation (GSI) analysis system has been employed in the current study.

The GSI analysis system developed by NOAA is supported for the community by the Joint Center for Satellite Data Assimilation (JCSDA) partners. The GSI replaced the current operational NCEP spectral statistical interpolation (SSI) global analysis system (Derber *et al*., 1991; Parrish and Derber 1992; Xu *et al*., 2008) by the regional DA system in May 2007. The main difference with respect to the SSI is that the DA system replaces the spectral definition for background errors with a grid point definition based on recursive filters that permit more degrees of freedom in defining the error statistics adaptively. The GSI is linked to the WRF-ARW mesoscale system, and the Advanced (TIROS)-N [Television and Infrared Observation Satellite] Operational Vertical Sounder (ATOVS) radiance observations are employed. The ATOVS radiance datasets show (Figure 8) that AMSU-A has the largest number (350) and covers most of the study areas, but the number in the AMSU-B radiance is only 95, and its coverage is beyond the Chinese mainland.

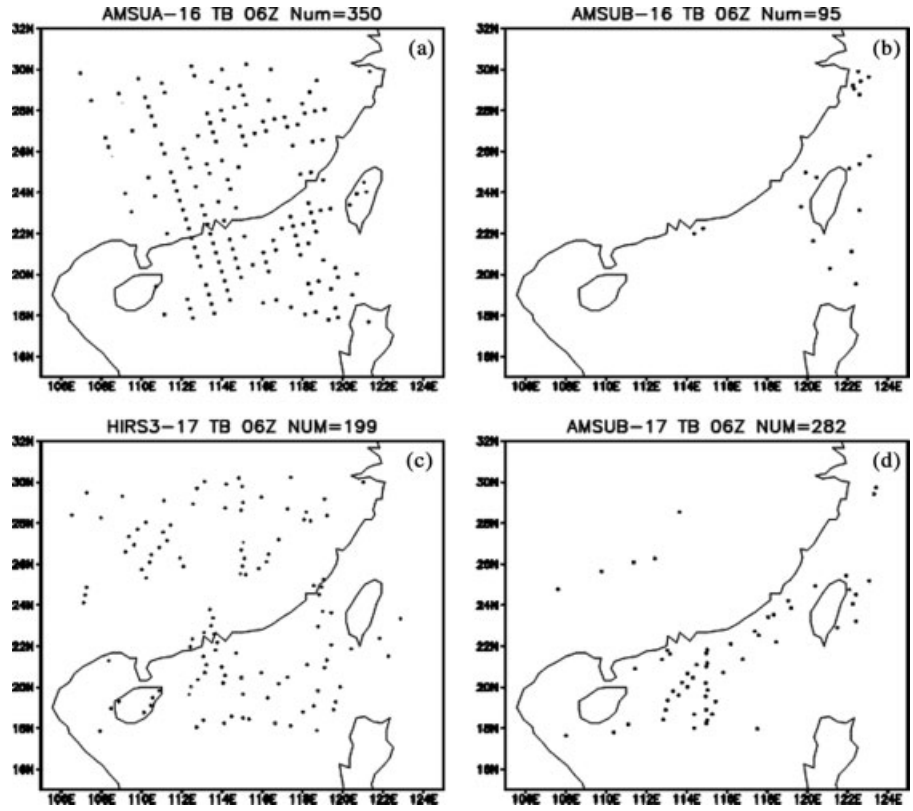

Figure 8. ATOVS (AMSU-A/B and (HIRS)/3) radiances have being used in current DA system at 06Z20 June 2005. (a) AMSU-A NOAA-16; (b) AMSU-B NOAA-16; (c) HIRS/3 NOAA-17 and (d) AMSU-B NOAA-17

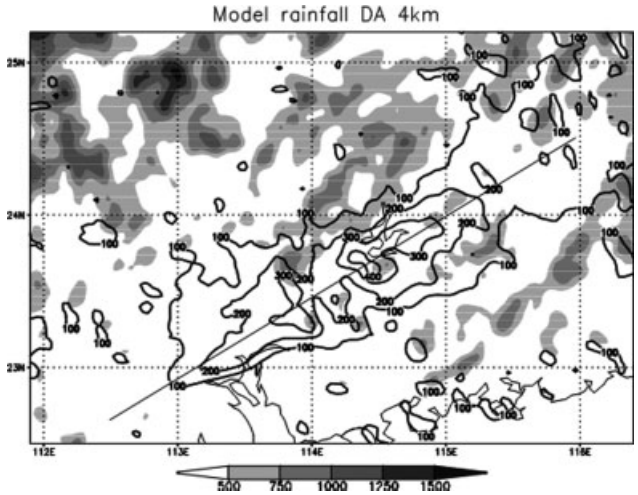

Figure 9. Simulated 24-h accumulated rainfall with the ATOVS radiance data assimilation from 06Z20 to 06Z21 June 2005. The model resolution and physical schemes options are the same as those in Figure 5a and the other definition is the same as that in Figure 2b

The 24-h accumulated precipitation in the DA experiment shows that the DA improved the rainfall distribution (Figure 9) to a large extent and corrected the maximum rainfall centre into the right position within the Xingfengjiang region. The axis of the rainband from the south-west to north-east was reproduced, although it did not completely match the observation (Figure 2b). The DA also produces a closer rainfall amount over the observed flooding area.

OBSERVATION OF THE RAINSTORMS AND PRECIPITATION

On the basis of the hourly satellite cloud-top infrared (IR) brightness temperature (T_{bb}), we used a standard ($-54\,^{\circ}$C isothermal line with a 20-km-diameter circle) to measure the activities of the meso-β rainstorm. At 18Z20 June, a standard circle of the isothermal line was initiated over the flooding region near the point (24°N, 114°E), which is a meso-β rainstorm (Figure 10a). There was another meso-β rainstorm 60 km to the west. During the subsequent 1 h, the eastern storm expanded to the east (Figure 10b). Starting from 20Z, the storm system developed individually and the lower T_{bb} decreased to below $-72\,^{\circ}$C (Figure 10c). By 22Z, the central intensity reached its maximum (Figure 10e). After 23Z, the diameter of the $-54\,^{\circ}$C isothermal circle increased up to 200 km, which is the standard for the meso-α convective system (Maddox, 1980). Meanwhile, the areas of $-72\,^{\circ}$C included several single meso-β rainstorms with diameters from ~30 to ~80 km (Figure 10f–h).

Corresponding to the development of the meso-β rainstorm in T_{bb}, the hourly precipitation distribution is shown in Figure 10i–p, in which the 10 mm h^{-1} rain rate is the standard to measure the activity of the meso-β rainstorm. At 18Z20 June, over the central flood region, two single meso-β rainstorms can be found: one over the north of the reservoir and another 55 km to the west (Figure 10i). Subsequently, the intensity of the western storm grew quickly (Figure 10j) and merged into the eastern one (Figure 10k) at 20Z20 June. The intensity of

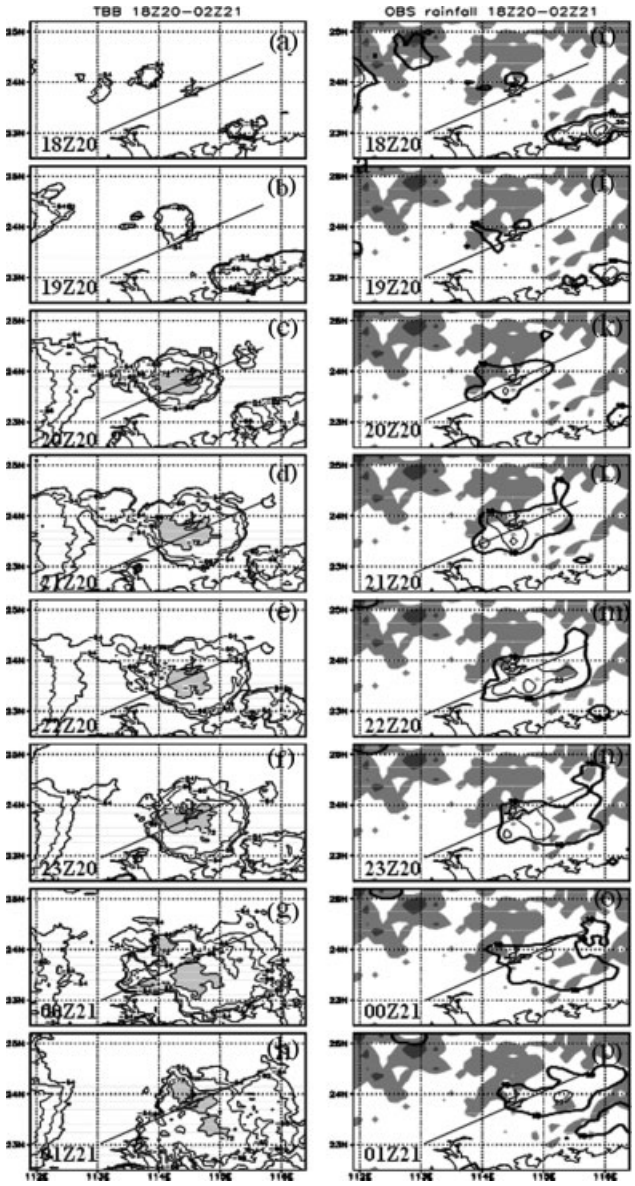

Figure 10. Observed evolution of satellite cloud-top IR blackbody temperature (T_{bb}: °C) and hourly rainfall (mm) from 18Z20 June 2005 to 01Z21 June 2005. T_{bb} (Left panel): (a) 18Z20, (b) 19Z20, (c) 20Z20, (d) 21Z20, (e) 22Z20, (f) 23Z20, (g) 00Z21 and (h) 01Z21. Areas of T_{bb} lower than −72 °C are shaded and the area of T_{bb} lower than −54 °C is contoured. Rainfall (right panel): (i) 18Z20, (j) 19Z20, (k) 20Z20, (L) 21Z20, (m) 22Z20, (n) 23Z20, (o) 00Z21 and (p) 01Z21. Areas of terrain elevation greater than 500 m are shaded (right panels). The slope line indicates the axis of the rain band in Figure 2b

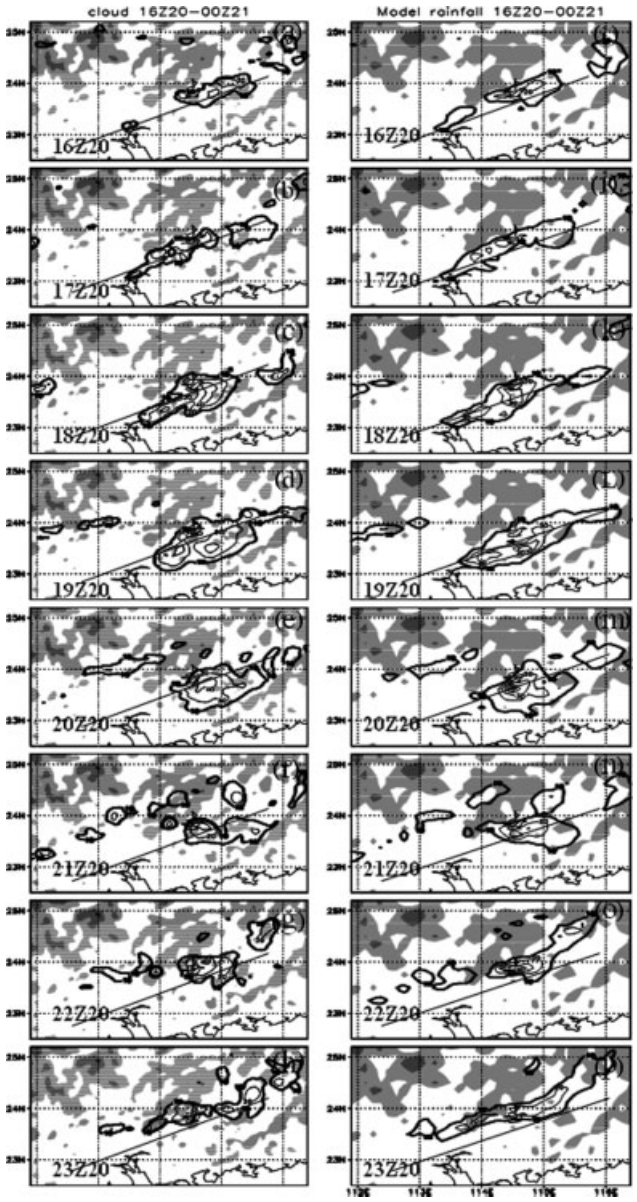

Figure 11. Modelled evolution of column cloud water and vapour (g kg^{-1}) and hourly rainfall (mm) from 16Z20 to 23Z20 Jun 2005. Cloud (Left panel): (a) 16Z20, (b) 17Z20, (c) 18Z20, (d) 19Z20, (e) 20Z20, (f) 21Z20, (g) 22Z20 and (h) 23Z20. Areas of column cloud water and vapour greater than 10 (g/kg) are plotted. Rainfall (right panel): (i) 16Z20, (j) 17Z20, (k) 18Z20, (L) 19Z20, (m) 20Z20, (n) 21Z20, (o) 22Z20, and (p) 23Z20. Areas of rain rate greater than 10 mm h^{-1} are plotted. The others are the same as those in Figure 10

the storm increased steadily and it moved slowly eastward until around 01Z21 June.

THE MODEL SIMULATION

Evolution of simulated rainstorm

The subsequent discussion is based on the simulation of the 4-km resolution model with the options of Eta Ferrier microphysics scheme, new Kain–Fritsch cumulus scheme and the initialization of satellite radiance DA. Corresponding to the observed cloud represented by T_{bb} (Figure 10), the simulated cloud is described by the column cloud water and vapour, in which the value of 10 g kg^{-1} is the standard to measure the activity of the meso-β rainstorm. In terms of the standard, the meso-β rainstorm initiated from 16Z20 June, 2 h earlier than the observation (Figure 11a). At 17Z, the 10 g kg^{-1} contour was separated into two meso-β rainstorms (Figure 11b): one moving quickly to the east of the Xingfengjiang region and the other to the south. At 20Z, the western storm (Figure 11e) moved eastward continuously and reached its maximum, whereas the eastern one moved out. Subsequently, the western storm reduced substantially (Figure 11f–h).

With the same standard as that observed in Figure 10i–o, the simulated precipitation shows (Figure 11i–o) that the simulation reproduced the rainfall pattern at each step of the development of the meso-β rainstorm. The 10-mm h^{-1} rain rate in the meso-β rainstorm was initiated at 16Z20 June (Figure 11i). With the development of the meso-β rainstorm, the rain rate got its maximum at 20Z20 June (Figure 11m). Subsequently, the rain rate decreased significantly with the reduction in the meso-β rainstorm.

On the basis of the rainfall distribution, the positions and tracks of the meso-β rainstorms in both observation and simulation are plotted in Figure 12. The results show that the meso-β rainstorms started from the foothill of Jiulian Mountain and moved slowly south-eastward; after reaching its maximum at 20Z20 June, the storms moved north-eastward with reduced intensity, although a certain degree of difference existed in the positions and tracks of the storms in observation and simulation.

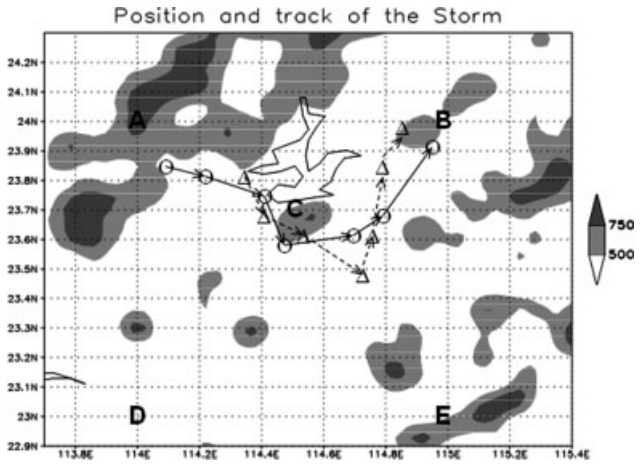

Figure 12. The positions and tracks of meso-β storms in simulation ('△' and dished line) and observation ('○' and solid line). 'C' represent the storm centre, and 'A, B, D and E' represent the four corner points. The central bird-like contour indicates the reservoir in the Xingfengjiang region

Structure of the rainstorms at the mature stage

According to above results, we took the model time at 20Z20 June 2005 as the mature stage, when the rain rate reached its maximum (Figure 11m). The positions of the two meso-β rainstorms (β1 and β2) are highlighted by shading (Figure 13a).

Mesoscale horizontal flow. At 850 hPa, the south-westerly dominates over the Xingfengjiang region and the surrounding mountain areas (Figure 13a) and the synoptic-scale LLJ with a wind speed of 12 m s^{-1} covers most of the areas of south-east China. On the basis of the criteria of a mesoscale system, the wind flow with a speed of 18 m s^{-1} is defined as the mesoscale low-level jet (MLLJ). By this definition, there are two single MLLJs in the midst of the synoptic LLJ, and both are located to the south-west of the storms β1 and β2, respectively (Figure 13a). At 300 hPa, a south-westerly with a wind speed of 12 m s^{-1} covers the region of the meso-β rainstorms (Figure 13b). Evidence shows that the south-westerly jet is tilted towards the north-east and its wind speed decreases with height.

For the divergence field, two convergence cells appeared over the south-western portion of the storm β1 at 850 hPa (Figure 14a) and one divergence cell occupied its north-eastern portion. A convergence cell dominated over the storm β2. Its counterpart at 300 hPa was roughly opposite (Figure 14b) over the two meso-β rainstorms. At the same time, a positive vortex occupied both meso-β rainstorms at 850 hPa, although there were two or more tiny vortexes embedded inside (Figure 14c) the storms. At 300 hPa, a pair of positive and negative vertexes appeared over storm β1, and the positive vortex was still over storm β2.

Moisture and temperature. For the dew-point temperature field (Figure 15a and b), the highest value always appeared to be close to the region over the meso-β rainstorms at either 850 or 300 hPa. Meanwhile, the high value of the moist static energy (MSE) dominated

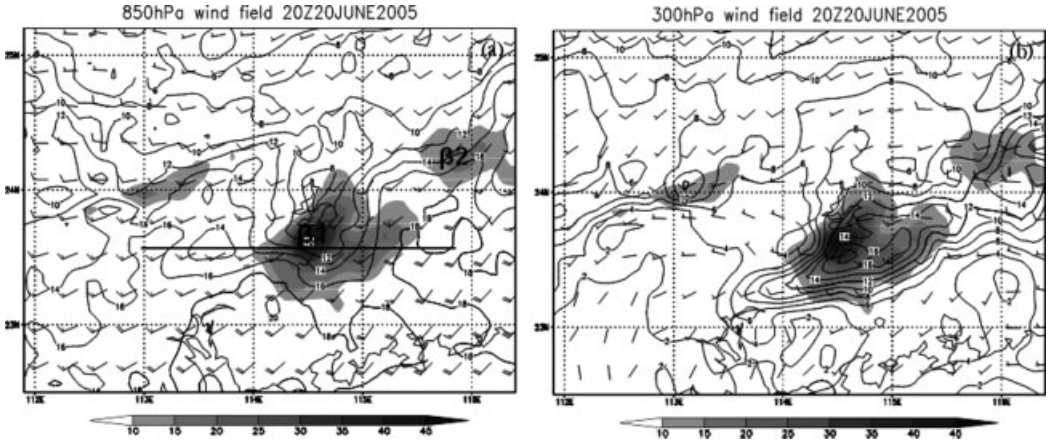

Figure 13. Winds at (a) lower (850 hPa) and (b) upper (300 hPa) level at the mature stage of meso-β storms (20Z20 June 2005). Contours are wind speed (m s^{-1}). The shading represents rain rate greater than 10 mm h^{-1}. β1 and β2 represents two single meso-β storms, respectively. The solid line indicates the position going through the centre of storm β1

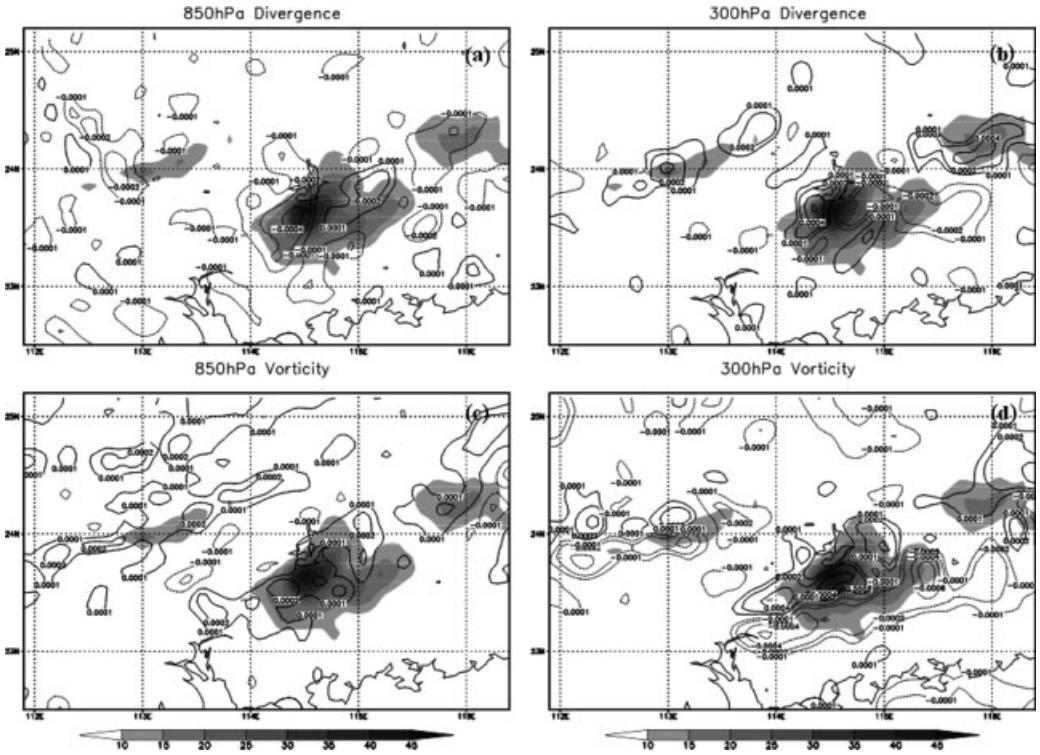

Figure 14. (a) 850 hPa divergence (s^{-1}), (b) 300 hPa divergence, (c) 850 hPa vorticity (s^{-1}) and (d) 300 hPa vorticity at the mature stage of the storm (20Z20 June 2005). The shading is the same as that in Figure 13

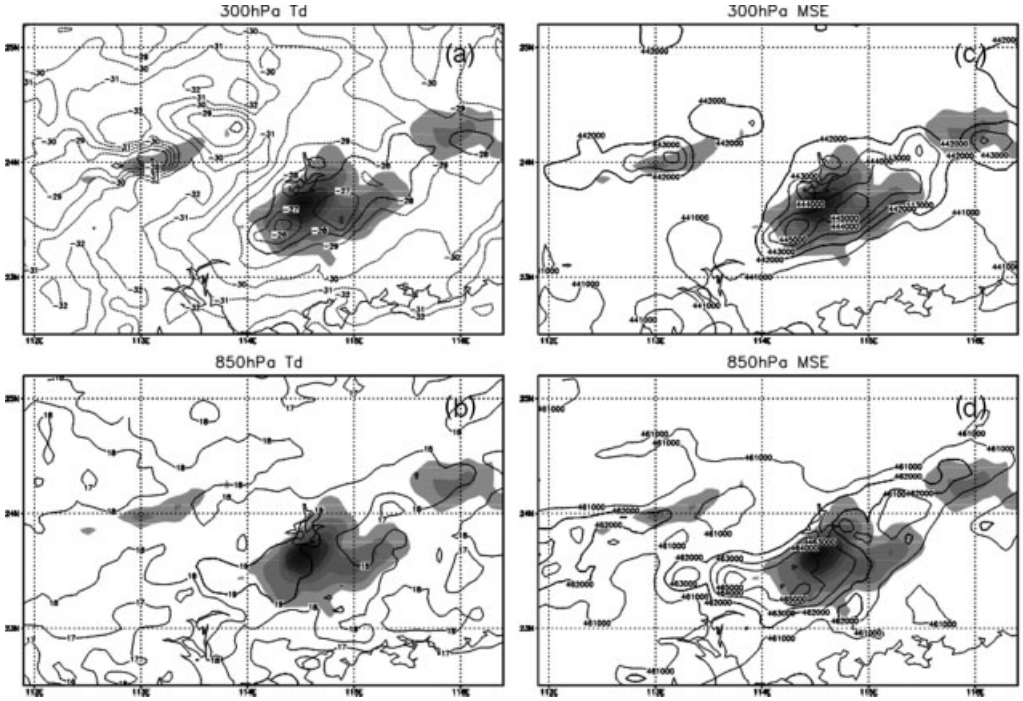

Figure 15. Dew-point temperature and MSE on lower (850 hPa) and upper (300 hPa) level at mature stage of the storm (20Z20 June 2005). (a) 300 hPa dew-point temperature (contour: °C), (b) 300 hPa MSE (contour: J g^{-1}), (c) 850 hPa dew-point temperature and (d) 850 hPa MSE. The shading is the same as that in Figure 13

over the storm centre at both low and middle levels (Figure 15c and d).

Vertical flow. With regard to the complication in the above storms $\beta 1$ and $\beta 2$, a longitude-pressure section through the centre of the storm $\beta 1$ (13·65 °N in Figure 13a) is plotted in Figure 16. Both the rain rate and the terrain elevation through the latitude are described in Figure 16 (bottom) with a curve line and a shaded bar, respectively. It is clear that the maximum rainfall of the storm $\beta 1$ was located over the western slope of a small mountain with height of ~700 m. The vertical

motion observed strong ascending of the storm with the maximum speed of 2·5 m s^{-1} at the vicinity of 500 hPa emerging from the west side of the maximum rainfall centre (Figure 16). The axis of the vertical speed tilted westward with height. To the east of the small mountain, the vertical motion was complicated with an updraft (downdraft) of over (under) 400 hPa. Apparently, the vertical motion was consistent with the rainfall of meso-β rainstorm, and it was affected significantly by the configuration of the local mountain, although the height of the mountain was less than 1000 m. The asymmetric vertical structure over the up and down slopes of the small mountain needs to be explored.

Thermodynamics. How can the meso-β rainstorms be maintained over the narrow mountain valley areas (Figure 12)? The five model grid-simulated soundings (A–E in Figure 12) represent the centre and the four corners of the storm β1 at 20Z (Figure 17). The results show that the strongest CAPE was not consistent with the storm centre (C) and was located at the south-west of the storm (D). There was a very weak CIN towards the centre of the storm (as indicated by the lifted parcel at the top of the boundary layer) at both the south and north sides and the CIN was much higher (A, B, E). Over the centre of the storm, the model-predicted boundary layer also had a substantial conditional instability. However, in contrast to the mountain sounding (A), there was a layer of fairly substantial CIN (102 J) above the boundary layer. The outflows predicted in the simulation were apparently not strong or deep enough to lift the boundary layer air through the layer of inhibition.

THE RELATIONSHIP BETWEEN RAINSTORM AND MESOSCALE LOW-LEVEL JET

Ding *et al*. (1992) noted that an LLJ is often observed and is highly correlated with the precipitation, in particular, with the heavy rainfall during the summer monsoon season. On the basis of the statistics of the relationship between the LLJ and heavy rainfall in the Guangdong Province using data for May–June of 1970–1973, Huang (1986) found that out of the 19 cases with an LLJ, 16 were accompanied by heavy rainfall. But this only reflected the relationship between the synoptic-scale LLJ and the rainstorm. The role of the MLLJ described in Figure 13a in this flash-flood event is worth discussing. For this, we examined the evolution of the rainstorms, dew-point temperature and the wind fields at 850 hPa, as well as the surface CAPE and CIN from an hourly model output.

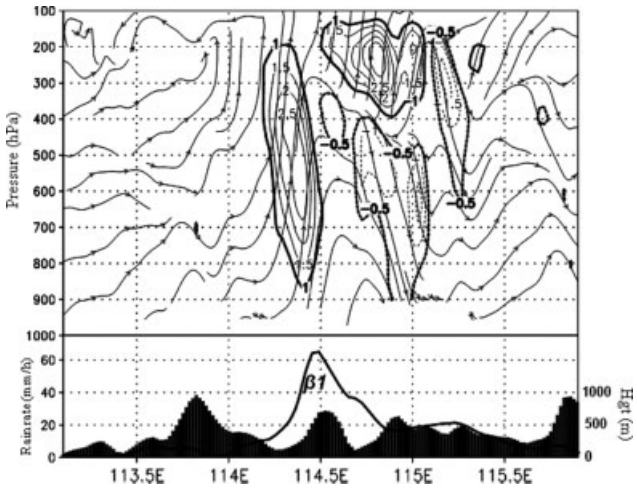

Figure 16. Longitude-pressure section of vertical motion through the rainstorm centre at 23·65 °N. Upper panel: contour indicates the vertical wind component (w: 0·1 m s^{-1}); stream field indicates the flow of zonal wind u with vertical wind $w \times 10$. Lower panel: shading represents the height of terrain (m) and the curve indicates the rain rate (mm h^{-1})

At 16Z (Figure 18a), the synoptic LLJ with a wind speed of 12 m s^{-1} had already covered most of the study areas and the MLLJ with a wind speed of 18 m s^{-1} just appeared sporadically to the south of the meso-β rainstorms. The generation of the MLLJ was closely associated with the development of the synoptic LLJ over south-east China. It should be noted that the highest dew-point temperature was associated with the higher moisture content located over the south-west side of storm β1, the south-westerly flow was directed towards the storm and a moist air belt (shading areas) was observed around the rainband. One hour later (Figure 18b), the wind speed increased substantially and the MLLJ was formulated significantly towards the south-west of this storm, and the high dew-point temperature centre increased, signalling the development of the storm. At 18Z (Figure 18c), associated with the development of storm β1, the MLLJ developed remarkably. Subsequently, the high dew-point temperature centre increased and moved eastward by 19Z (Figure 18d). The volume of warm, moist air feeding into the storm enhanced the development of storm β1 to a mature stage, whereas another MLLJ occurred over the south-west of storm β2.

At 20Z (Figure 18e), when the storm β1 was in a mature stage, the MLLJ increased continuously. The high dew-point temperature tended to decrease and moved northward. It should be noted that the MLLJ did not stop increasing after the mature stage had been reached and the wind speed increased to 21 m s^{-1} at 21Z (Figure 18f). Two hours later (Figure 18h), the MLLJ predominated the whole south of the meso-β rainstorms. As the south-westerly MLLJ penetrated into the storm, a high moisture content centre formed and was consistent with the storm.

The result obtained here is different from the relationship between heavy rainfall events and the synoptic-scale LLJ in the Guangdong area described in the study of Huang (1986). He noted that about 84·2% of the heavy rainfall events were accompanied by a synoptic LLJ, which existed for 1–5 days before the start of heavy rain (Ding 1992). In this case, the synoptic-scale LLJ also existed before the development of rainstorms. However, the interaction between the storms and MLLJ is more complicated. The MLLJ promoted the development of meso-β rainstorms before the mature stage of the storm was reached; subsequently, the MLLJ increased steadily with reduction in the storm.

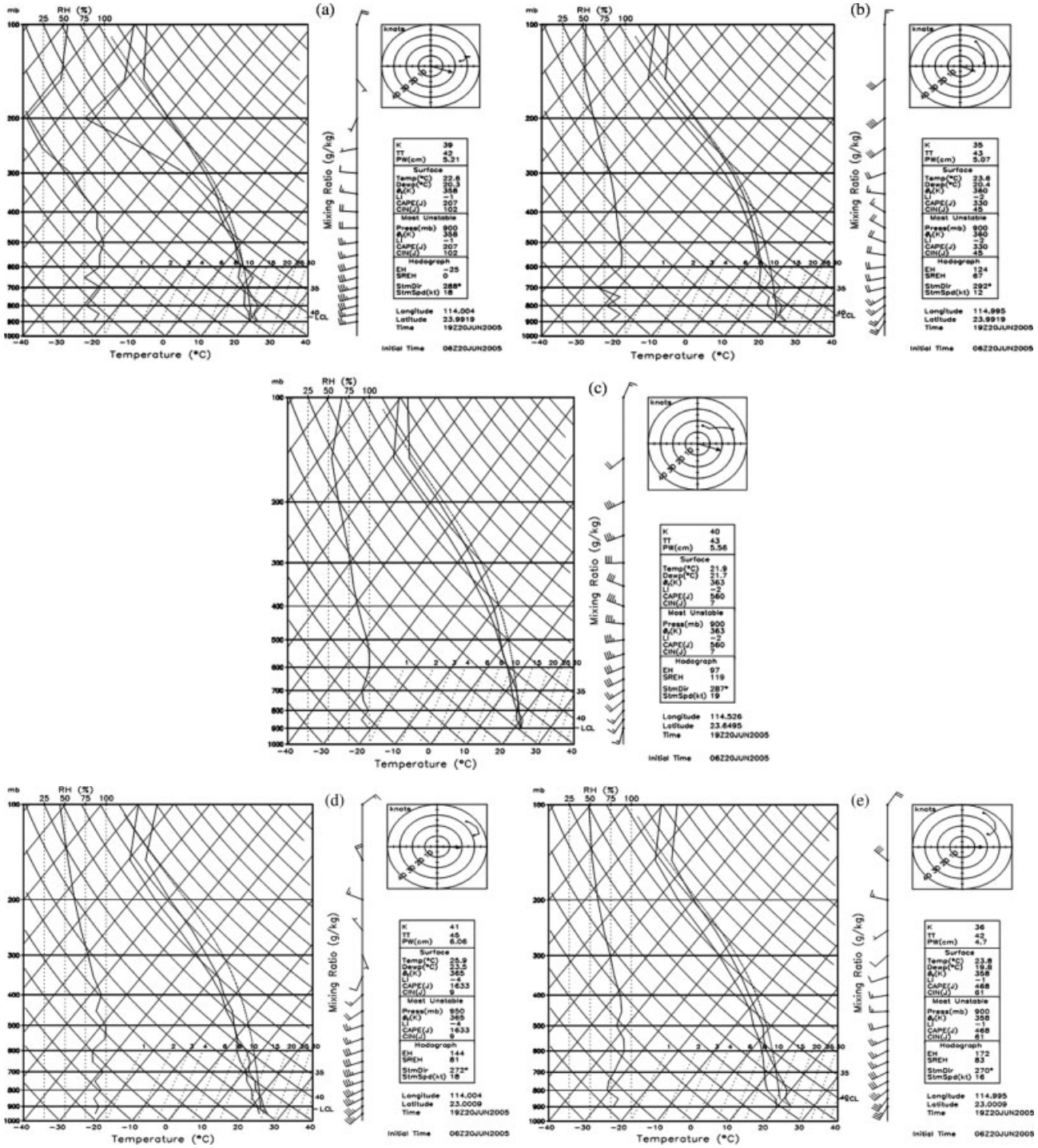

Figure 17. Upper-air sounding at centre point (C) and four corner points (A, B, D, E) at the mature phase (06Z20 June 2005) around the storm β1. The five grid points are indicated in Figure 12

However, with the development of MLLJ towards the north-east, the eastern meso-β rainstorms, such as storm β2, did not develop; contrarily, it seems that the rainfall was trapped in the region of storm β1 (Figure 12). What is the reason for this trapping? To answer this question, the variation of the CAPE and CIN at the five representative positions described in Figures 12 and 17 is discussed. The results (Figure 19) show that the surface CAPE (left panels in Figure 19) at the storm centre (grid point C) is in agreement with the evolution of the storm β1, and reached its maximum at the mature stage at 20Z, then the CAPE decreased substantially; meanwhile, an opposite variation could be found in CIN (right panels in Figure 19). Compared to the value of the CAPE over the other four corners, we found that the central CAPE was coming from the south-west region (D) and remained high over the storm central areas, which indicated a development at the rear of storm's eastward movement. On the other hand, the fairly higher CIN appearing over the other three places surrounding the activities of the

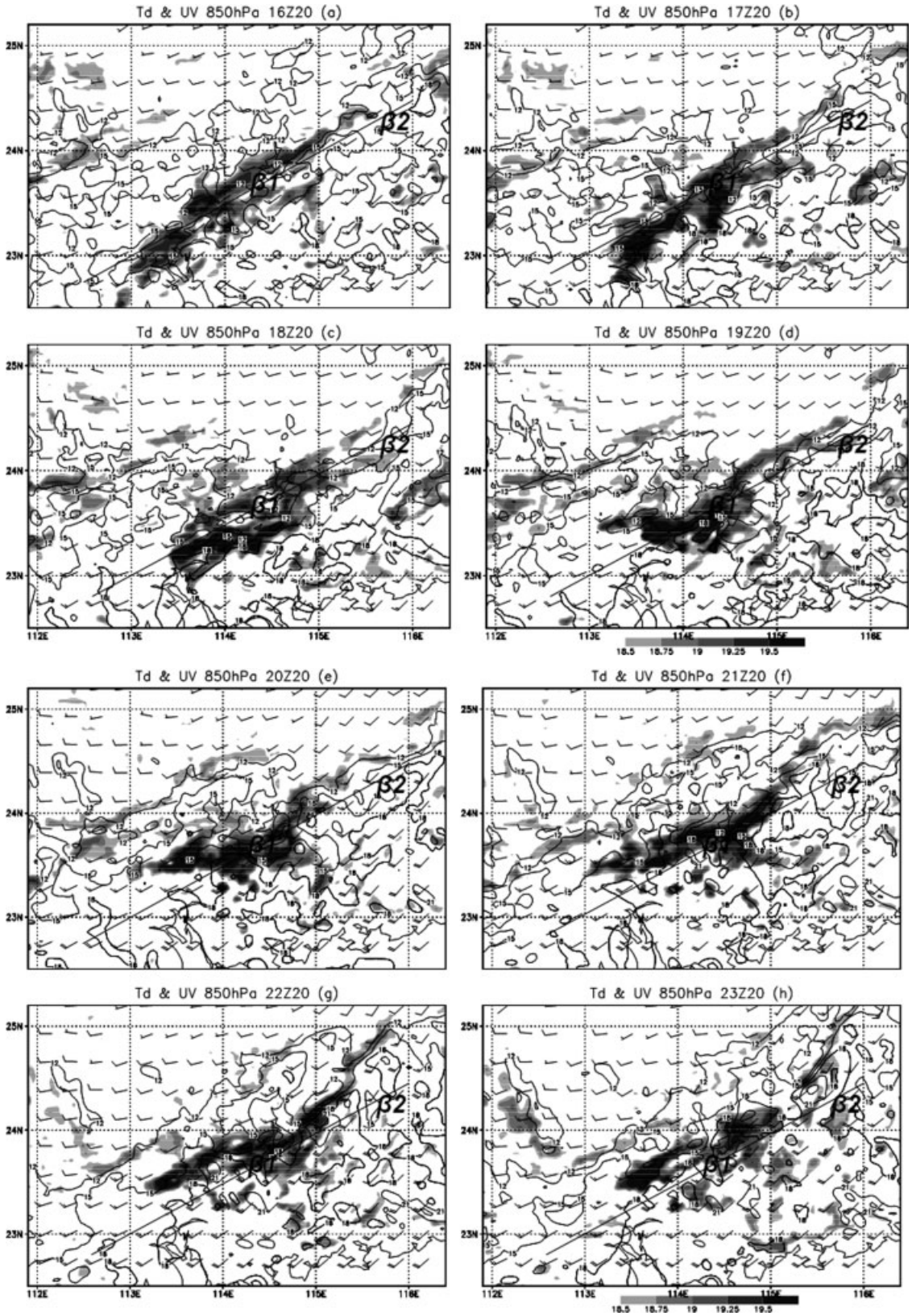

Figure 18. Evolution of dew-point temperature (shaded with great than 18·5 °C) and wind flow at 850 hPa (contour: wind speed greater than 12 m s^{-1}) from 16Z20 to 23Z20 Jun 2005. The heavy contour with wind speed of 18 m s^{-1} indicates the MLLJ. (a) 16Z20, (b) 17Z20, (c) 18Z20, (d) 19Z20, (e) 20Z20, (f) 21Z20, (g) 22Z20 and (h) 23Z20. 'β1 and β2' indicate the location of the meso-β storms at the mature stage in Figure 13. The slope line indicates the axis of the rain band in Figure 2b

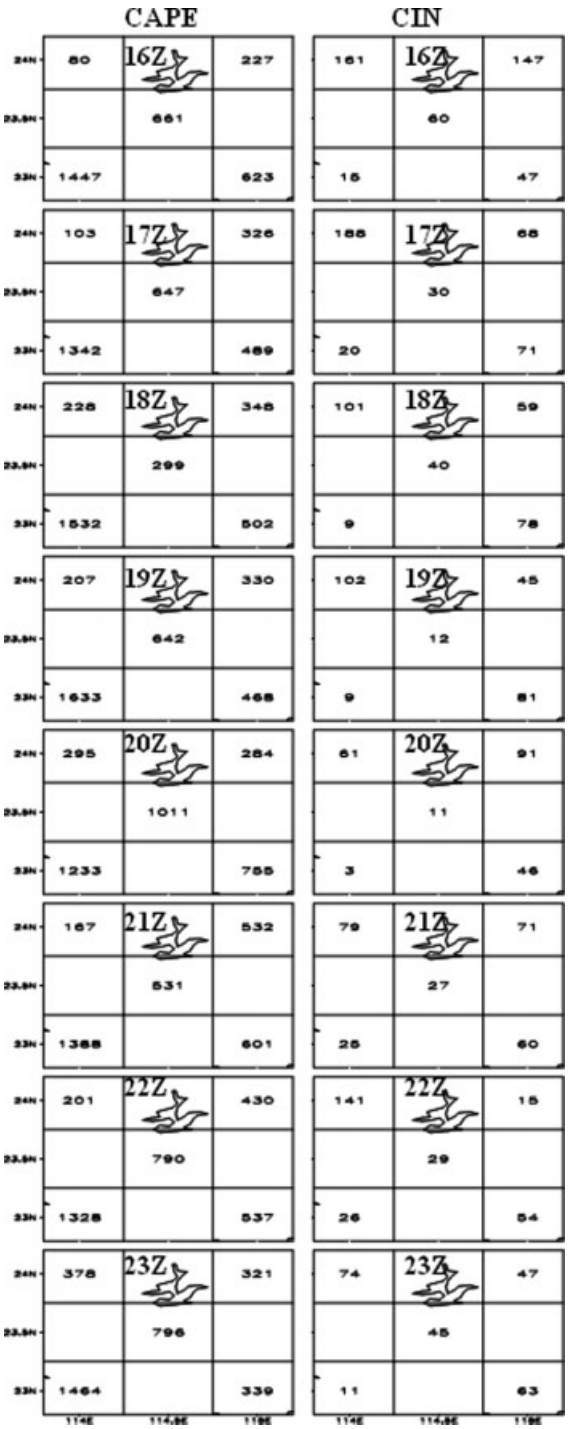

Figure 19. Evolution of CAPE (in J, left panel) and CIN (in J, right panel) at five grid points (A–E) around rainstorm in Figure 12 from 16Z20 to 23Z20 Jun 2005. The central area with bird-like contour indicates the reservoir in the Xingfengjiang region

storm prohibited the unstable energy from moving out of the areas.

SUMMARY

The evolution and structure of meso-β rainstorms associated with a flash-flood event are simulated using the NCAR mesoscale model (ARW-WRF). The event was based on a flash flood that occurred in the Guangdong Province of south-east China during 20–21 June 2005. Comparing the hourly mixed rain-gauge and satellite-retrieved precipitation data, the model was able to reproduce growth and merger of meso-β rainstorm.

The results indicated that the persistent development of meso-β rainstorms was maximum evidence associated with each phase of the strong convective storm in the flash flood. The model-predicted rain rate, however, was overestimated slightly, and the activities of the storms did not precisely correspond with the observed, although the peak values were obtained. The model-simulated convection occurred about 2 h early.

The structure of the meso-β rainstorm in the mature phase was investigated. At 300 hPa, the convective storm was embedded within the high dew-point temperature domain. Several meso-β rain cells were positioned inside the convective storm and the high MSE value dominated. At 850 hPa, the highest dew-point temperature was lying towards approximately 50 km west of the meso-β rainstorm. The vertical motion was significantly affected by the local mountain and displayed an asymmetric vertical structure over the up and down slopes of the small mountain.

The south-westerly MLLJ defined by a wind speed of 18 m s^{-1} carrying abundant moisture to the south of rain belt from South China Sea and Bay of Bengal provided the primary condition for the rainstorm. All simulated meso-β rainstorms were initiated over and moved slowly near the central Xingfengjiang region. However, the interaction between the meso-β rainstorms and MLLJ is very complicated. The MLLJ promoted the development of meso-β rainstorms before the mature stage of the storm was reached. The CAPE was released towards the central areas of the rainstorm to provide a beneficial condition for the development of the convective system, but it was trapped within an area surrounded by the northern Julian, southern Lianhua and eastern small mountains, resulting in the occurrence of the severe flash flood.

ACKNOWLEDGEMENTS

Authors would like to thank the Joint Center for the Satellite Data Assimilation (JCSDA) for providing the GSI data assimilation system. This study was supported by the National Key Science and Technology Program of China under Grant 2006BAC02B and by the Meteorological Specific Research under Grant GYHY200706014.

REFERENCES

Betts AK, Miller MJ. 1986. A new convective adjustment scheme. Part II: single column tests using GATE wave, BOMEX, and arctic air-mass data sets. *Quarterly Journal of the Royal Meteorological Society* **112**: 693–709.

Chen S-J, Kuo Y-H, Wang W, Tao Z-Y, Cui B. 1998. A modeling case study of heavy rainstorms along the Mei-Yu front. *Monthly Weather Review* **126**: 2330–2351.

Derber JC, Wu W-S. 1998. The use of TOVS cloud-cleared radiances in the NCEP SSI analysis system. *Monthly Weather Review* **126**: 2287–2299.

Ding Y-H. 1992. Summer monsoon rainfalls in China. *Journal of the Meteorological Society of Japan* **70**: 337–396.

Dudhia J. 1989. Numerical study of convection observed during the winter monsoon experiment using a mesoscale two-dimensional model. *Journal of the Atmospheric Sciences* **46**: 3077–3107.

Fang Z. 1985. The preliminary study of medium-scale cloud cluster over Changjiang basin in summer. *Advances in Atmospheric Sciences* **2**: 334–340.

Ferrier B. 1994. A double-moment multiple-phase four-class bulk ice scheme. Part I: description. *Journal of the Atmospheric Sciences* **51**: 249–280.

Gallus WA Jr. 1999. Eta simulations on three extreme precipitation events: sensitivity to resolution and convective parameterization. *Weather and Forecasting* **14**: 405–426.

Gallus WA, Bresch James F. 2006. Comparison of impacts of WRF dynamic core, physics package, and initial conditions on warm season rainfall forecasts. *Monthly Weather Review* **134**: 2632–2641.

Giorgi F, Shields C. 1999. Tests of precipitation parameterizations available in latest version of NCAR regional climate model (RegCM) over continental United States. *Journal of Geophysical Research* **104**: 6353–6357.

Grell GA, Devenyi D. 2002. A generalized approach to parameterizing convection combining ensemble and data assimilation techniques. *Geophysical Research Letters* **29**(14): 1693. DOI: 10.1029/2002GL015311.

Hong S-Y, Pan H-L. 1996. Nonlocal boundary layer vertical diffusion in a medium-range forecast model. *Monthly Weather Review* **124**: 2322–2339.

Hong S-Y, Juang H-MH, Zhao Q. 1998. Implementation of prognostic cloud scheme for a regional spectral model. *Monthly Weather Review* **126**: 2621–2639.

Hong S-Y, Dudhia J, Chen S-H. 2004. A revised approach to ice microphysical processes for the bulk parameterization of clouds and precipitation. *Monthly Weather Review* **132**: 103–120.

Huang SS. 1986. *The Presummer Heavy Rainfall over South China*. Guangdong Science and Technology Press: China; 243 pp (in Chinese).

Joyce RJ, Janowiak JE, Arkin PA, Xie P. 2004. CMORPH: a method that produces global precipitation estimates from passive microwave and infrared data at high spatial and temporal resolution. *Journal of Hydrometeorology* **5**: 487–503.

Kain JS, Fritsch JM. 1993. Convective parameterization for mesoscale models: the Kain–Fritcsh scheme. In *The Representation of Cumulus Convection in Numerical Models*, Emanuel KA, Raymond DJ (eds). Amer. Meteor. Soc.: United States; 246. pp.

Kessler E. 1969. *On the distribution and continuity of water substance in atmospheric circulation*. *Meteor. Monogr.* 32. Amer. Meteor. Soc.: United States; 84 pp.

Lorenz EN. 1963. The mechanics of vacillation. *Journal of the Atmospheric Sciences* **20**: 448–465.

Li J, Maddox RA, Gao X, Sorooshian S, Hsu K. 2003. A numerical investigation of storm structure and evolution during the July 1999 Las Vegas flash flood. *Monthly Weather Review* **131**: 2038–2059.

Lin Y-L, Farley RD, Orville HD. 1983. Bulk parameterization of the snow field in a cloud model. *Journal of Climate and Applied Meteorology* **22**: 1065–1092.

Maddox RA, Canova F, Hoxit LR. 1980. Meteorological characteristics of flash flood events over the western United States. *Monthly Weather Review* **108**: 1866–1877.

Mass CF, Ovens D, Westrick K, Colle BA. 2002. Does increasing horizontal resolution produce more skillful forecasts?. *Bulletin of the. American Meteorological Society* **83**: 407–430.

McAnelly RL, Cotton William R. 1986. Meso-β-scale characteristics of an episode of meso-α-scale convective complexes. *Monthly Weather Review* **114**: 1740–1770.

Mlawer EJ, Taubman SJ, Brown PD, Iacono MJ, Clough SA. 1997. Radiative transfer for inhomogeneous atmosphere: RRTM, a validated correlated-k model for the longwave. *Journal of Geophysical Research* **102**(D14): 16663–16682.

Parrish DF, Derber JC. 1992. The National Meteorological Center's spectral statistical interpolation analysis system. *Monthly Weather Review* **120**: 1747–1763.

Skamarock WC, Klemp JB, Dudhia J, Gill DO, Barker DM, Wang W, Powers JG. 2005. A description of the advanced research WRF version 2. NCAR Tech. Note NCAR/TN-468+STR; 94. pp.

Thompson G, Rasmussen RM, Manning K. 2004. Explicit forecasts of winter precipitation using an improved bulk microphysics scheme. Part I: description and sensitivity analysis. *Monthly Weather Review* **132**: 519–542.

Wang W, Seaman NL. 1997. A comparison study of convective parameterization schemes in a mesoscale model. *Monthly Weather Review* **125**: 252–277.

Weisman ML, Shamarock WC, Klemp JB. 1997. The resolution dependence of explicitly modeled convective systems. *Monthly Weather Review* **125**: 527–548.

Xu J, Small EE. 2002. Simulating summertime rainfall variability in the North American monsoon region: the influence of convection and radiation parameterizations. *Journal of Geophysical Research* **107**(D23): 4727. DOI: 10.1029/2001JD002047.

Xu J, Gao X, Sorooshian S. 2006. The influence of assimilating rainfall derived from WSR-88D radar on the rainstorm forecasts over the south western United States. *Journal of Geophysical Research* **111**: D13105. DOI: 10.1029/2005JD006650.

Xu J, Rugg S, Horner M, Byerle L, Liu Z, Barker D. 2009. Application of ATOVS radiance with ARW WRF/GSI data assimilation system in the prediction of hurricane Katrina. *The Open Atmospheric Sciences Journal* **3**: 13–28.

Zhang DL, Fritsch JM. 1986. A case study of the sensitivity of numerical simulation of mesoscale convective systems to varying initial conditions. *Monthly Weather Review* **114**: 2418–2431.

Zhang Q, Lau KH, Kuo YH, Chen SJ. 2003. A numerical study of a mesoscale convective system over the Taiwan Strait. *Monthly Weather Review* **131**: 1150–1170.

Zhu Q-G, Lin J-R, Shou S-W. 1981. *Principles and Methods in Synoptic Meteorology*. Beijing Meteorological Press: China; 535 pp. (in Chinese).

